ACSNANO

www.acsnano.org

ARTICLE

# Coherence Programming for Efficient Linearly Polarized Perovskite Light-Emitting Diodes

Meiqin Xiao, Jonghee Yang,* Wei Zhang,* Long Xu, Jidong Zhang,* Wenzhe Li,* Chen Chen, Tingwei Zhou, Haoyue Zhang, Bo Chen, Junzhong Wang, and Ping Chen*

Cite This: https://doi.org/10.1021/acsnano.4c11761 Read Online

ACCESS | Metrics & More | Article Recommendations | Supporting Information

**ABSTRACT:** Although quasi-two-dimensional (quasi-2D) perovskites are ideal material platforms for highly efficient linearly polarized electroluminescence owing to their anisotropic crystal structure, so far, there has been no practical implementation of these materials for the demonstration of linearly polarized perovskite light-emitting diodes (LP-PeLEDs). This scarcity is due to difficulty in orientation and phase distribution control of the quasi-2D perovskites while minimizing the defects, all of which are required to manifest aligned transition dipole moments (TDMs). To achieve this multifaceted goal, herein, we introduce a synergistic strategy to quasi-2D perovskites by incorporating both a trimethylolpropane triacrylate anchoring layer and 18-Crown-6 molecular passivator into the film fabrication process. It is found that the interfacial anchoring layer guides the oriented growth of perovskites along the (110) plane, whereas the molecular passivator reduces the number of defects and homogenizes the crystal phase. As a result, a quasi-2D perovskite film with macroscopically aligned TDM that renders high radiative recombination and the degree of linear polarization (DoLP) is constructed. This "coherence-programmed emission layer" demonstrates highly efficient LP-PeLEDs, not only achieving a maximum external quantum efficiency of ~23.7%, a brightness of ~36,142 cd/m$^2$, and a DoLP of ~38%, but also significantly improving the signal-to-interference-and-noise ratio in a multicell visible light communication system.

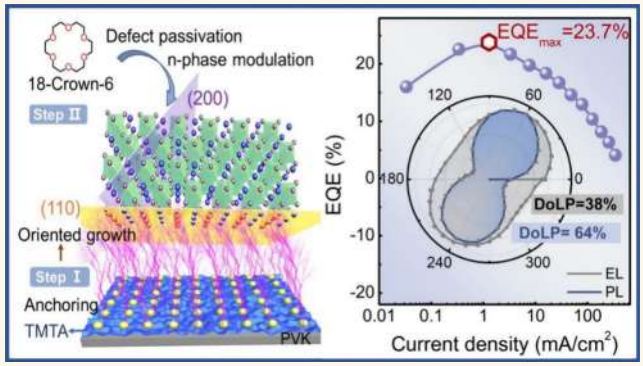


**KEYWORDS:** *quasi-2D perovskites, light-emitting diodes, linearly polarized, oriented growth, passivation*

## INTRODUCTION

Linear polarization of electroluminescence (EL) from light-emitting diodes (LEDs) is essential in emerging applications such as holographic stereoscopic imaging,[1−5] visible light communication (VLC),[6] and so on.[7,8] To develop linearly polarized LEDs, great efforts have been made either on integration of optics elements (e.g., waveguides[9] or polarizer[8]) outside the LEDs or modifications of luminescent materials (e.g., using magnetic atoms[10] or auxiliary layer[11]). However, these strategies not only result in the complex designs of optical systems and their meticulous manipulation but also cause severe light loss in operation. These considerably curtail the actual LED's efficiency, which subsequently limits the imaging quality of polarized light.

An effective solution is to use luminescent materials with intrinsic polarization characteristics. Metal halide perovskites have recently become rising stars in LED technologies, demonstrating outstanding performances owing to their excellent optoelectronic properties.[12−18] Another advantage of these promising materials stems from their feasibility in dimensional tailoring of the crystals that bestow the structural anisotropy.[19−23] These anisotropic structures manifest the coherent alignment of radiative transition dipole moments (TDMs) along the longitudinal axis, thereby leading to linearly polarized light emission.[2,8] From this perspective, indeed, progress has been realized in various low-dimensional perovskite nanomaterials manifesting distinct linearly polarized photoluminescence (PL), such as nanowires,[21,24,25] nanosheets,[26] and so on.[27,28] However, it is still challenging to demonstrate high performances in linearly polarized EL—achieving both high efficiency and degree of linear polarization (DoLPs)—from the perovskite-based LEDs (PeLEDs) with such low-dimensional nanostructures.[26] Up to date, the maximum external quantum efficiency (EQE$_{max}$) and max-

Received: August 25, 2024
Revised: September 26, 2024
Accepted: October 2, 2024

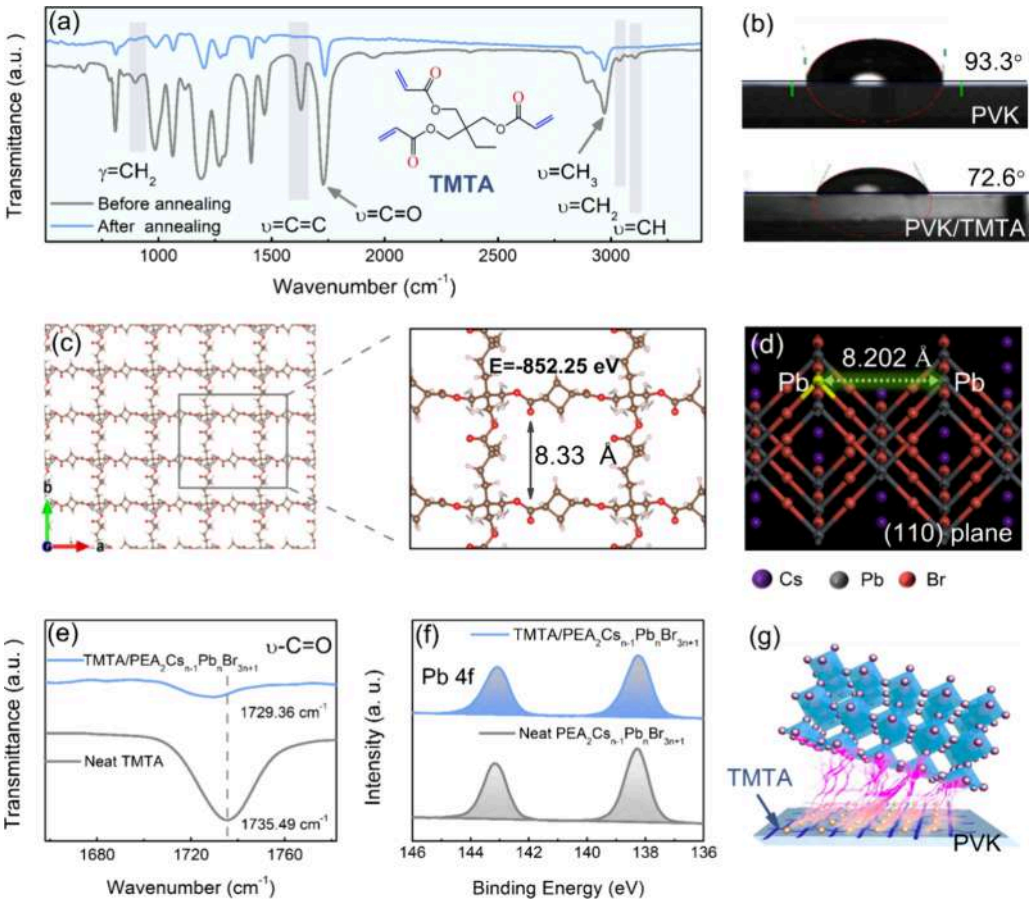


**Figure 1. (a) FTIR spectra of TMTA films before (gray) and after (blue) annealing. The gray rectangular areas indicate the characteristic vibration peaks of TMTA. (b) Water contact angles of PVK and PVK/TMTA films. (c) Most stable periodic grid structure formed by cross-linking of TMTA monomers with the lowest formation energy. (d) Lattice structure of the (110) plane in $CsPbBr_3$. (e) FTIR spectra of neat TMTA and TMTA/$PEA_2Cs_{n-1}Pb_nBr_{3n+1}$ films. (f) Pb 4f core-level XPS spectra of neat TMTA and TMTA/$PEA_2Cs_{n-1}Pb_nBr_{3n+1}$ films. (g) Schematic illustration of oriented growth of perovskite along the (110) direction by the TMTA anchoring layer.**

imum luminance ($L_{max}$) of reported linearly polarized perovskite light-emitting diodes (LP-PeLEDs) based on mechanically rubbing-aligned $CsPbBr_3$ nanowires,[29] thickness-controlled $CsPbBr_3$ single-crystal thin film,[30] and oriented superlattice $CsPbI_3$ nanosheets[26] are all below ~4% and ~4000 cd/m$^2$, respectively, making them far from the practical applications.

Quasi-two-dimensional (quasi-2D) perovskites, where the inorganic lattices are dimensionally confined within the planar space by molecular cations, are ideal material platforms for realizing polarized emission owing to their intrinsic structural and emission anisotropies. Additionally, quasi-2D perovskites exhibit high emission quantum yields attributed to high exciton binding energy and ultrafast energy/carrier funneling properties.[31−34] Together with their synthetic feasibility in the solution process as well as outstanding phase stability, it is anticipated that the use of quasi-2D perovskites offers high-performance LP-PeLEDs. Notwithstanding, such an opportunity has not been explored so far due to the (i) random-oriented crystal packing,[35,36] (ii) emergence of multiple 2D perovskite phases, and (iii) high defect densities in this materials system,[36] while factors (i) and (ii) impede the coherent alignment of emission TDMs, and the latter electrostatically shields the local TDMs.[37] As a consequence, the macroscopic coherence of TDMs across the perovskite thin films is dissipated unless all of these drawbacks are concurrently resolved, thereby leading to great difficulty in realizing linearly polarized EL.

To deal with this multifaceted problem, herein, we systematically program the coherence of TDMs in quasi-2D perovskites by implementing a synergistic crystal growth management approach. Primarily, we introduce cross-linked trimethylolpropane triacrylate (TMTA) as a lattice anchoring layer, which rigidly templates the oriented growth perovskite crystal lattice along the (110) direction by offering similar interfacial lattice constant while mitigating phase heterogeneities. Second, we use a molecular additive 18-Crown-6 into the precursor solutions, not only passivating the uncoordinated $Pb^{2+}$ defects on the perovskite surface through Lewis interactions but also homogenizing the phase distribution via promoted growth of the medium-$n$ ($n \geq 4$) 2D phases. This two-step strategy allows for the establishment of coherent TDM alignment across the quasi-2D perovskite thin films, thus offering high DoLPs and a high radiative recombination rate of medium-$n$ 2D phases.

Implementation of the "coherence-programmed" luminescent thin films to PeLEDs indeed demonstrates high performances in linearly polarized EL operations, achieving $EQE_{max}$, $L_{max}$, and DoLP of ~23.7%, ~36,142 cd/m$^2$, and ~38% respectively. Specifically, to best of our knowledge, this represents the highest efficiency of LP-PeLEDs reported to date (Table S1).[26,29,20,38] Also, upon utilization as active light


https://doi.org/10.1021/acsnano.4c11761
ACS Nano XXXX, XXX, XXX−XXX

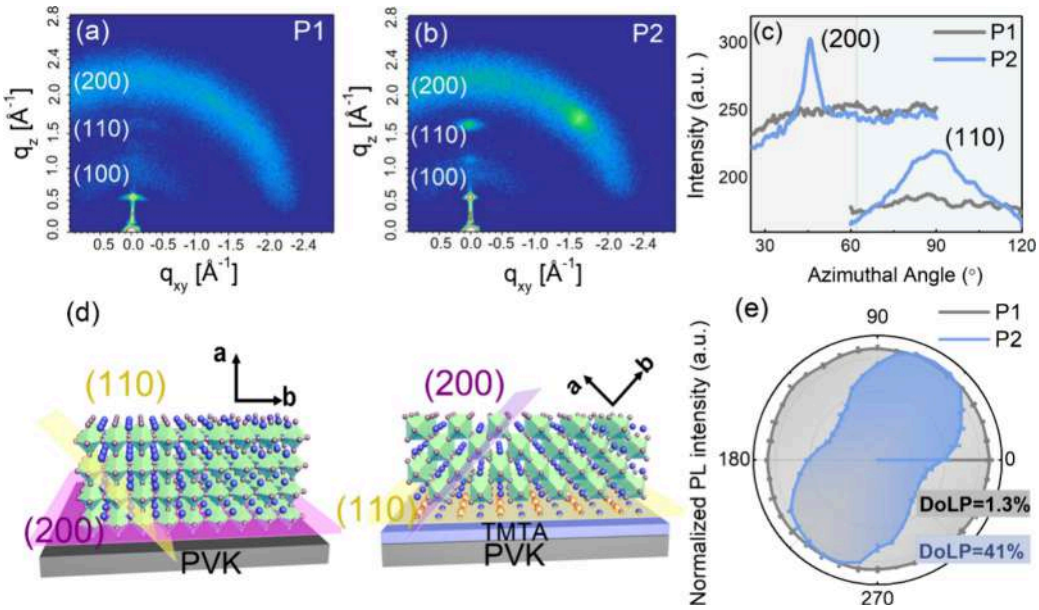


**Figure 2. GIWAXS patterns of (a) P1 and (b) P2 samples. (c) Azimuthal profile of (110) and (200) planes of P1 and P2 samples. (d) Schematic illustration showing the angle change between the (110) and (200) planes before and after the oriented growth of $CsPbBr_3$ crystals. (e) Polar plots of the polarized PL of P1 and P2 samples.**

sources for multicell visible light communication (MC-VLC), the LP-PeLEDs significantly improve signal-to-interference-and-noise ratio (SINR) compared to the nonpolarized PeLEDs.

## RESULTS AND DISCUSSION

The periodic network with anchoring properties of the substrates, which plays important roles in the oriented growth of perovskite crystallites,[39,40] is realized by the cross-linking of the TMTA monomers. Even at a relatively low temperature of ~140 °C, the cross-linking action of the TMTA monomers, particularly the connection of $CH_2{=}CH$ groups into $CH_2{-}CH_2$, can take place without involving detrimental effects on the underlying poly(*N*-vinylcarbazole) (PVK) hole transport layer (HTL). Fourier-transform infrared (FTIR) spectra of the neat TMTA film in Figure 1a confirm that characteristic peaks of $CH_2{=}CH$ including $\nu{=}CH$ (~3107 cm$^{-1}$), $\nu{=}CH_2$ (~3037 cm$^{-1}$), and $\gamma{=}CH_2$ (907 cm$^{-1}$) disappear upon thermal annealing. It is noted that the cross-linked TMTA offers a polar nature on the PVK surface due to the abundant C═O functional groups,[41] which is confirmed by the smaller water contact angle of ~72.6° on the TMTA/PVK thin film than ~93.3° on the PVK thin film, as shown in Figure 1b. This promotes oriented, heterogeneous crystal growth that has structural coherence across the film. Moreover, the cross-linked TMTA is no longer soluble in dimethyl sulfoxide (DMSO) (Figure S1), which ensures the stand of the TMTA film when spin-coating the perovskite precursor solution on top of it.

The resulting periodic structures of the cross-linked TMTA layer are studied by density function theory (DFT) calculations. The six possible periodic networks of TMTA after cross-linking are constructed with 164 atoms, which are sufficiently large to keep the simulations reasonable. Thereafter, the models are refined to the fine-optimized level, and the corresponding formation energies are obtained. We compared the structures and their formation energies in Figure S2 and Table S2. The most stable structure with the lowest formation energy is selected for studies, as shown in Figure 1c. In this structure, the spacing of adjacent C═O is found to be ~8.33 Å, which has a high lattice matching rate (~98%) to the neighbor $Pb^{2+}$-$Pb^{2+}$ spacing ~8.202 Å of the (110) plane in $CsPbBr_3$ crystals (Figure 1d).

Given such a periodic surface from the distinct molecular structure of the cross-linked TMTA layer, it can be envisaged that, upon crystallization, the $Pb^{2+}$ of the perovskites can be coordinated with C═O functional groups through Lewis interaction. Indeed, an appreciable downshift of the C═O stretching mode from 1735 to 1729 cm$^{-1}$ is observed on the TMTA/$PEA_2Cs_{n-1}Pb_nBr_{3n+1}$ film, indicating the presence of electrostatic interaction between TMTA and perovskites (Figure 1e). This is because the coordination of the lone pairs in the C═O bond toward $Pb^{2+}$ is deemed to cause a redistribution of electron density across the functional group. Specifically, such electron donation can lower the vibrational frequency of the C═O stretching mode.[42−44]

To gain atomic-scale insights into the chemical interaction between TMTA and the perovskite, Pb 4f core-level X-ray photoelectron spectroscopy (XPS) is performed on the corresponding films, as shown in Figure 1f. Compared to the neat $PEA_2Cs_{n-1}Pb_nBr_{3n+1}$ film, the spectra of the TMTA/$PEA_2Cs_{n-1}Pb_nBr_{3n+1}$ film shift to lower binding energy, indicating the higher charge density on $Pb^{2+}$ by electron transfer from C═O to $Pb^{2+}$.[41] Given the periodic C═O-functionalized surface with a lattice constant analogous to the perovskite (110) surface as well as its preferential coordination with uncoordinated $Pb^{2+}$ upon crystallization, it can be hypothesized that the cross-linked TMTA can promote the oriented growth of perovskites along the (110) direction, as schematically shown in Figure 1g.

To explore the crystal orientations in the $PEA_2Cs_{n-1}Pb_nBr_{3n+1}$ perovskite films, grazing-incidence wide-angle X-ray scatterings (GIWAXS) are performed.[45] Figure 2a shows the GIWAXS patterns of the neat $PEA_2Cs_{n-1}Pb_nBr_{3n+1}$ film (P1 sample), which exhibits three Debye−Scherrer diffraction rings at $q_z$ = 1.1, 1.53, and 2.1 Å$^{-1}$. These GIWAXS patterns agree well with the X-ray diffraction peaks (Figure S3)


https://doi.org/10.1021/acsnano.4c11761
ACS Nano XXXX, XXX, XXX−XXX

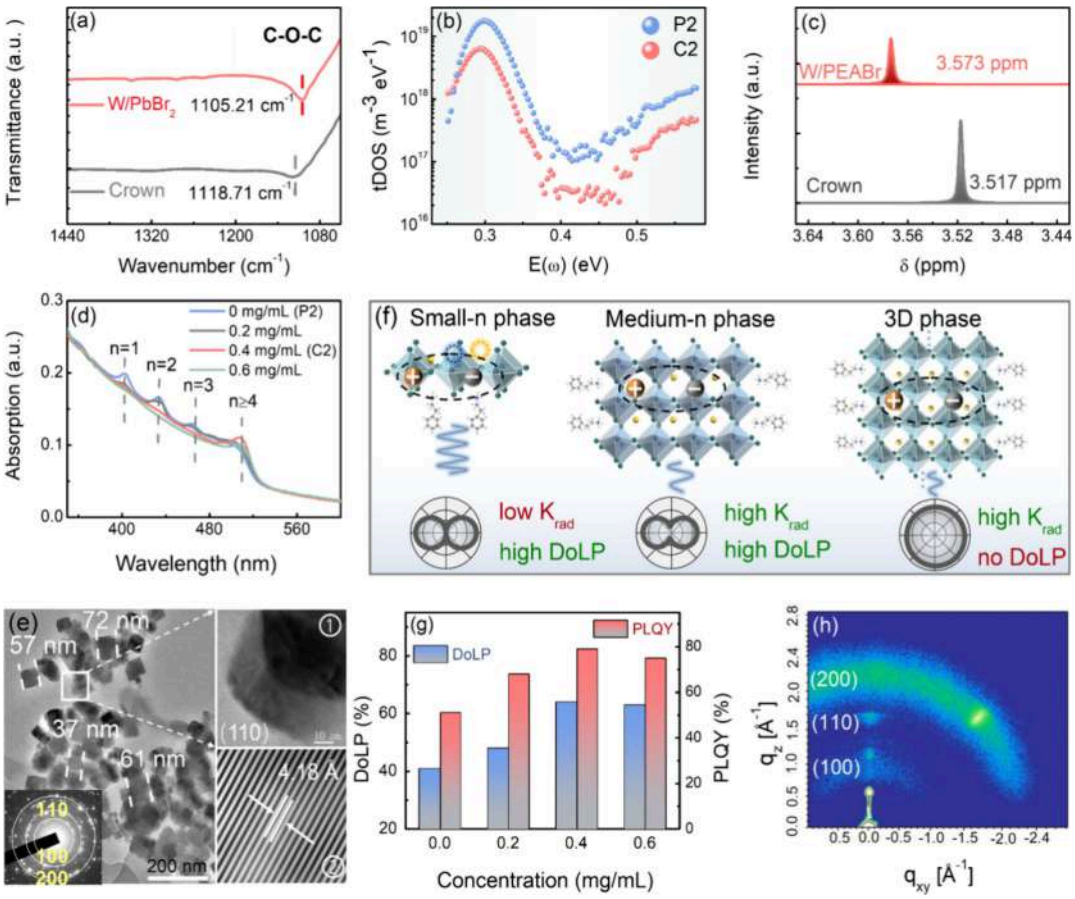


**Figure 3. (a) FTIR spectra for the neat 18-Crown-6 and 18-Crown-6:$PbBr_2$ films. (b) tDOS of the P2 and C2 samples. (c) $^1$H NMR spectra for neat 18-Crown-6 and 18-Crown-6:PEABr in deuterated DMSO. (d) Steady-state UV−vis absorption spectra of quasi-2D perovskite films with different concentrations of 18-Crown-6. (e) TEM images and SAED patterns of the crystals from the C2 sample. Insets ① and ② show the HR-TEM image and lattice fringes, respectively. (f) The schematic illustration shows the DoLP and recombination rate of small-*n* phase, medium-*n* phase, and 3D phase perovskite crystals. (g) DoLP and PLQY of quasi-2D perovskite films with different 18-Crown-6 concentrations. (h) GIWAXS patterns of the C2 film.**

at ∼15.6, 21.9, and 31.0°, corresponding to the (100), (110), and (200) planes of $PEA_2Cs_{n-1}Pb_nBr_{3n+1}$ crystals, respectively.[46] The isotropic and uniform intensity profiles of these rings indicate that the perovskite crystals in the P1 sample exhibit random-oriented crystallographic structures. In contrast, distinctive Braggs spots at $q_z$ = 1.53 and 2.1 Å$^{-1}$ along 90° (out-of-plane direction) and 45° are respectively observed in the TMTA/$PEA_2Cs_{n-1}Pb_nBr_{3n+1}$ film (P2 sample) (Figure 2b). Such oriented signatures that manifested in the P2 sample are more evident in the corresponding azimuthally integrated scattering intensities (Figure 2c), clearly demonstrating the oriented growths of the (110) and (200) planes along ∼90 and ∼45°, respectively. To quantify the fraction of the perovskite unit cells oriented favorably, the orientational order parameter *S* of the (110) plane is calculated for the P1 and P2 samples (Note S1), which are found to be −0.08 and −0.2, respectively. This strongly suggests that the anchoring action of cross-linked TMTA toward the perovskite precursor promotes the crystal growth along the perovskite (110) plane direction, as illustrated in Figure 2d.

The optical coupling outputs provide further evidence for the oriented growth of $PEA_2Cs_{n-1}Pb_nBr_{3n+1}$ crystals, as oriented growth promotes the establishment of aligned TDMs, leading to anisotropic emission.[26] Figure S4 shows the angle-dependent PL and EL profiles. Similar to the angular-dependent EL profiles, the PL intensity distribution of the P1 film remains almost unchanged within the collection angle from −90 to +90°, following Lambert's law. However, the P2 film exhibits a non-Lambertian profile with peak intensity at ∼±45°, indicating the establishment of TDMs aligning ∼45° with respect to the substrate.

The establishment of aligned TDMs in quasi-2D perovskite thin films favors the generation of linearly polarized light. To estimate the linear polarization degree of P1 and P2 samples, the DoLP is defined by eq 1:

$$\mathrm{DoLP} = (I_{max} - I_{min})/(I_{max} + I_{min}) \quad (1)$$

$I_{max}$ and $I_{min}$ represent the maximum and minimum PL or EL intensities after passing through the polarizer, respectively, which are obtained by the experimental setup in Figure S5. The DoLP values range from 0 to 100%, representing fully unpolarized to fully linearly polarized light emissions. As shown in Figure 2e, the DoLP of the P1 sample is only ∼1.3%, showing negligible linearly polarized light emission. In contrast, the DoLP of the P2 sample significantly increases to ∼41%, likely attributed to the establishment of aligned TDMs by oriented growth of $PEA_2Cs_{n-1}Pb_nBr_{3n+1}$ crystals.

Having explored the crystallographic orientation of the perovskite films, the influence of defects on the polarized emission from the quasi-2D perovskites is assessed. In


https://doi.org/10.1021/acsnano.4c11761
ACS Nano XXXX, XXX, XXX−XXX

principle, the TDMs are established by electron−hole pairs confined within the 2D plane.[47] Thus, TDMs are highly susceptible to local electric fields that are applied for photo- or electric excitations.[37] Perovskite thin films are deemed to have high defect densities due to solution processing. This allows for the generation of highly disordered and localized electric fields around those charged defects. As a consequence, the coherence of TDMs in quasi-2D perovskite thin films breaks, thus negating the linearly polarized light emission.

To address this shielding effect of local electric fields, 18-Crown-6 is incorporated into the precursor solutions to passivate the defects in $PEA_2Cs_{n-1}Pb_nBr_{3n+1}$ (C2 sample). FTIR spectra of neat 18-Crown-6 and 18-Crown-6:$PbBr_2$ films reveal that the chemical interaction between the precursor ions and 18-Crown-6 is prolonged after film crystallization. A downshift of C−O−C stretching mode from ∼1118.71 to 1105.21 $cm^{-1}$ is observed in Figure 3a, indicating that 18-Crown-6 molecules are participating in the perovskite surface chemistry via Lewis interaction toward uncoordinated $Pb^{2+}$.

We quantify the trap density of states (tDOS) in P2 and C2 samples using thermal emission spectroscopy (TAS), as shown in Figure 3b. Here, the tDOS values in the corresponding perovskite matrices are estimated through eq 2:[48]

$$N_T(E_\omega) = -\frac{V_{bi}}{qW}\frac{dC_p}{d\omega}\frac{\omega}{k_BT} \tag{2}$$

where $W$ and $V_{bi}$ are the depletion width and built-in potential, respectively, which are extracted from the capacitance−voltage ($C$−$V$) curves in Figure S6. Also, $C$, $\omega$, and $k_BT$ are the capacitance, frequency, and thermal energy, respectively, obtained from the capacitance−frequency ($C$−$F$) curves in Figure S7. The tDOS of the C2 device decreases about 1 order of magnitude lower than that of the P2 device, confirming the passivation effects of 18-Crown-6.

The time-resolved photoluminescence (TRPL) spectra are further obtained in Figure S8 and fitted by the three-exponential functions:[49]

$$I(t) = I_0 + A_1\exp(-t/\tau_1) + A_2\exp(-t/\tau_2) + A_3\exp(-t/\tau_3) \tag{3}$$

where $A_1$, $A_2$, and $A_3$ are amplitudes, and $\tau_1$, $\tau_2$, and $\tau_3$ are fast, medium, and slow decay lifetime constants associated with surface and volume trap-assisted radiative recombination and the bimolecular radiation recombination inside the crystal grain, respectively. The fitting parameters are summarized in Table S3. The increased $\tau_1$ and $\tau_3$ of the C2 sample suggest that 18-Crown-6 effectively passivates the defects of $PEA_2Cs_{n-1}Pb_nBr_{3n+1}$ perovskites, thereby inhibiting the defect-assisted nonradiative recombination and enhancing the radiative recombination.

It is found that the incorporation of 18-Crown-6 not only passivates the uncoordinated $Pb^{2+}$ but also modulates the $n$-phase distribution of the quasi-2D perovskites.[50] This can be attributed to the hydrogen bonds formed between 18-Crown-6 and PEABr, as confirmed by the solution-phase $^1$H nuclear magnetic resonance ($^1$H NMR) spectra in Figure 3c. Compared to neat 18-Crown-6, appreciable downfield chemical shifts of $-CH_2$ protons are observed from ∼3.517 to ∼3.583 ppm when PEABr is incorporated into the solutions, indicating the reduced electron density at the corresponding protons as a result of the interaction between the ammonium head of cationic species and oxygen in 18-Crown-6 ether. Therefore, the coordination capability of PEABr to the perovskite framework is reduced, leading to the inhibition of fast formation of small-$n$ phases (e.g., $n$ = 1, 2, and 3 phases) but the promotion of medium-$n$ phases ($n \geq 4$).[51] To gain more insights into the phase homogenization in the $PEA_2Cs_{n-1}Pb_nBr_{3n+1}$ perovskite film, UV−vis absorption spectra are collected (Figure 3d). The P2 sample exhibits four absorption peaks at ∼400, 432, 463, and 505 nm, corresponding to the excited states of $n$ = 1, 2, and 3 and $n \geq 4$ phases, respectively.[52] As the concentration of 18-Crown-6 increases to ∼0.4 mg/mL, the excitonic peaks of the small-$n$ phases are suppressed, whereas the $n \geq 4$ peak becomes significantly enhanced. Note that no appreciable changes in these absorption peaks are observed by further increasing the 18-Crown-6 concentration to ∼0.6 mg/mL, suggesting that the phase modulation action is saturated at ∼0.4 mg/mL. Steady-state PL spectra also confirm the phase modulation action upon the incorporation of 18-Crown-6 (Figure S9), where the emissions from the $n$ = 1, 2, and 3 phases are suppressed, but the emission from $n \geq 4$ phases is enhanced by 18-Crown-6.

To explore the structural properties of the coherence-programmed $PEA_2Cs_{n-1}Pb_nBr_{3n+1}$ crystallites at the atomic scale, transmission electron microscopy (TEM) images of the C2 sample are collected, as shown in Figure 3e. The crystals exhibit cubic crystals with uniform sizes from ∼20 to 30 nm, indicating homogenization of $n \geq 4$ phases.[51] The selected-area electron diffraction (SAED) patterns in the inset of Figure 3e clearly indicate three diffraction rings of the (100), (110), and (200) planes,[53] agreeing well with the GIWAXS and XRD patterns. High-resolution TEM images show uniform diffraction streaks, and the spacing of the lattice fringe is found to be ∼0.418 nm, aligning with the (110) plane of cubic phases of $CsPbBr_3$.

Such $n \geq 4$ phases of quasi-2D perovskites are ideal for high-performance LP-PeLEDs, as illustrated in Figure 3f. This is because, although small-$n$ phases (e.g., $n$ = 1, 2, and 3) with anisotropic structures can generate high-degree linearly polarized light emission, the strong electroacoustic coupling will make the high energy of small-$n$ phase be easily quenched by the vibrational levels from defects.[51] Thus, nonradiative recombination is usually observed in small-$n$ phases.[23,54] But for the 3D phases (e.g., $n \sim \infty$) with an isotropic structure, their DoLPs are quite low despite the high radiative recombination rates.[37] Compared to small-$n$ and 3D phases, the medium-$n$ phase ($n \geq 4$) crystals simultaneously possess high radiative recombination and high DoLP of the quasi-2D perovskites. Following this strategy, medium-$n$ phases are modulated by 18-Crown-6. Effects of 18-Crown-6 concentrations on DoLP and PLQY are revealed in Figure 3g. From 0 to ∼0.4 mg/mL, the DoLP and PLQY increase from ∼41 and ∼38% to ∼64 and ∼79%, respectively. These enhancements are primarily due to the promotions of the medium-$n$ phases by 18-Crown-6. Further increasing the concentration to ∼0.6 mg/mL cannot further improve DoLP and PLQY (Figure 3d), again suggesting that the phase regulation and passivation actions of 18-Crown-6 are already saturated at this concentration. It is important to note that the 2D GIWAXS patterns of the C2 sample replicate that of the P2 sample (Figure 3h), corroborating that the oriented growth of $PEA_2Cs_{n-1}Pb_nBr_{3n+1}$ perovskites is not compromised by using 18-Crown-6. Here, the two-step strategies synergistically manifest the coherence of TDMs across the perovskite matrix,


https://doi.org/10.1021/acsnano.4c11761
ACS Nano XXXX, XXX, XXX−XXX

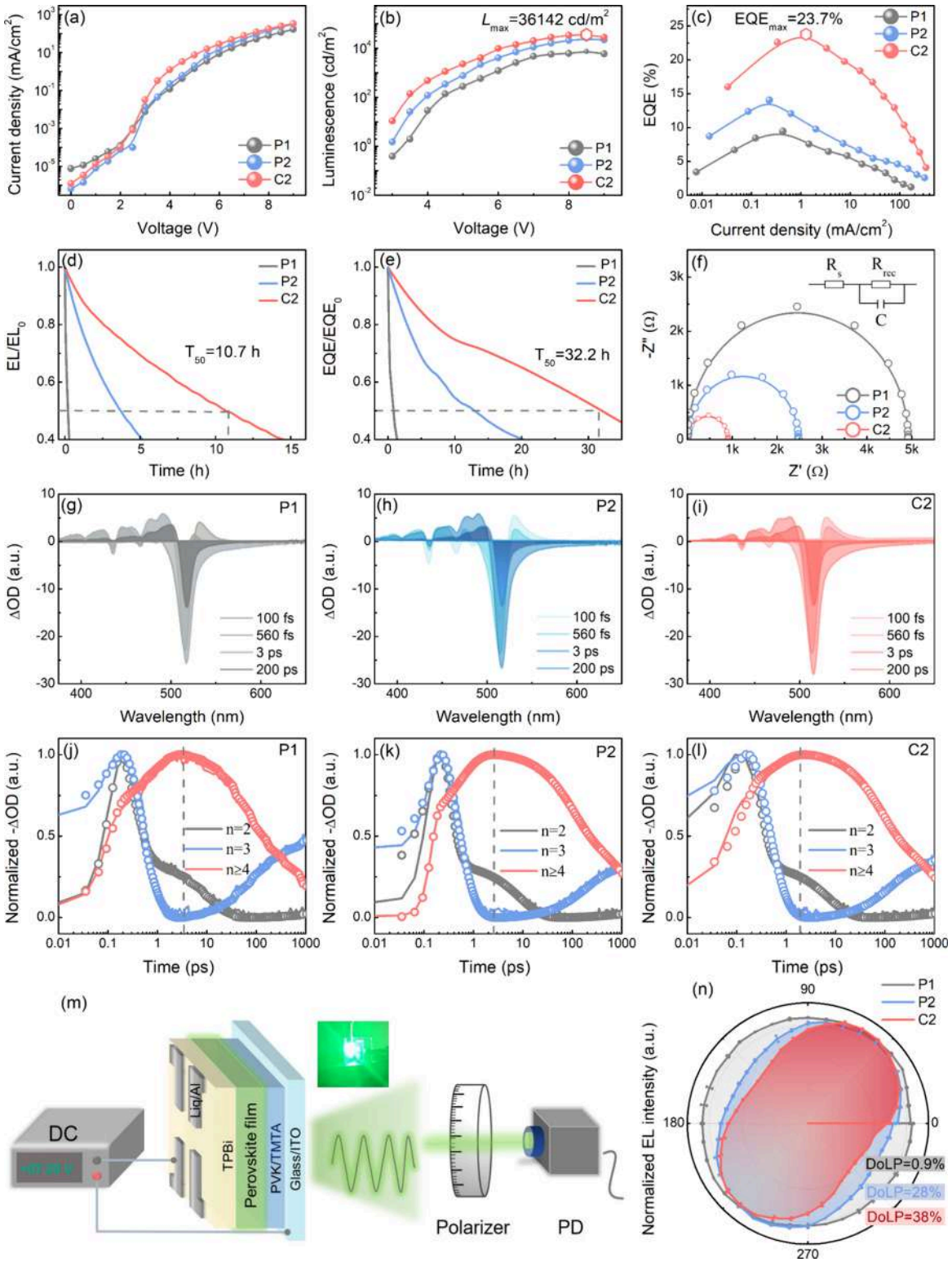


**Figure 4. $J$−$L$−$V$ characteristics of fabricated PeLEDs including (a) $J$−$V$, (b) $L$−$V$, and (c) EQE−$J$ characteristics. (d) EL/EL$_0$ and (e) EQE/EQE$_0$ for $T_{50}$ measurements of the PeLEDs. (f) Nyquist plots of the P1, P2, and C2 devices from EIS measurements at an applied bias of 3.5 V. fs-TA spectra of (g) P1, (h) P2, and (i) C2 samples at selected time scales of 100 fs, 560 fs, 3 ps, and 200 ps. GSB decay kinetics probed at selected wavelengths for $n$ = 2 and 3 and $n \geq 4$ phases for (j) P1, (k) P2, and (l) C2 samples, respectively. (m) Experimental setup for measuring the DoLP of EL. (n) Polar plots of the polarized EL of P1, P2, and C2 devices.**

thus ensuring efficient polarized EL by demonstrating PeLEDs with this coherence-programmed emitter matrix.

By using the P1, P2, or C2 thin films as the emitting layer, the PeLEDs with a layered structure of indium tin oxide (ITO)/PVK with or without a TMTA layer/quasi-2D perovskite with or without 18-Crown-6/1,3-tris(1-phenyl-19H-benzo[d]-imidazol-2-yl)benzene (TPBi)/hydroxyquinolinatolithium (Liq)/Al are fabricated, as shown in Figure S10.


https://doi.org/10.1021/acsnano.4c11761
ACS Nano XXXX, XXX, XXX−XXX

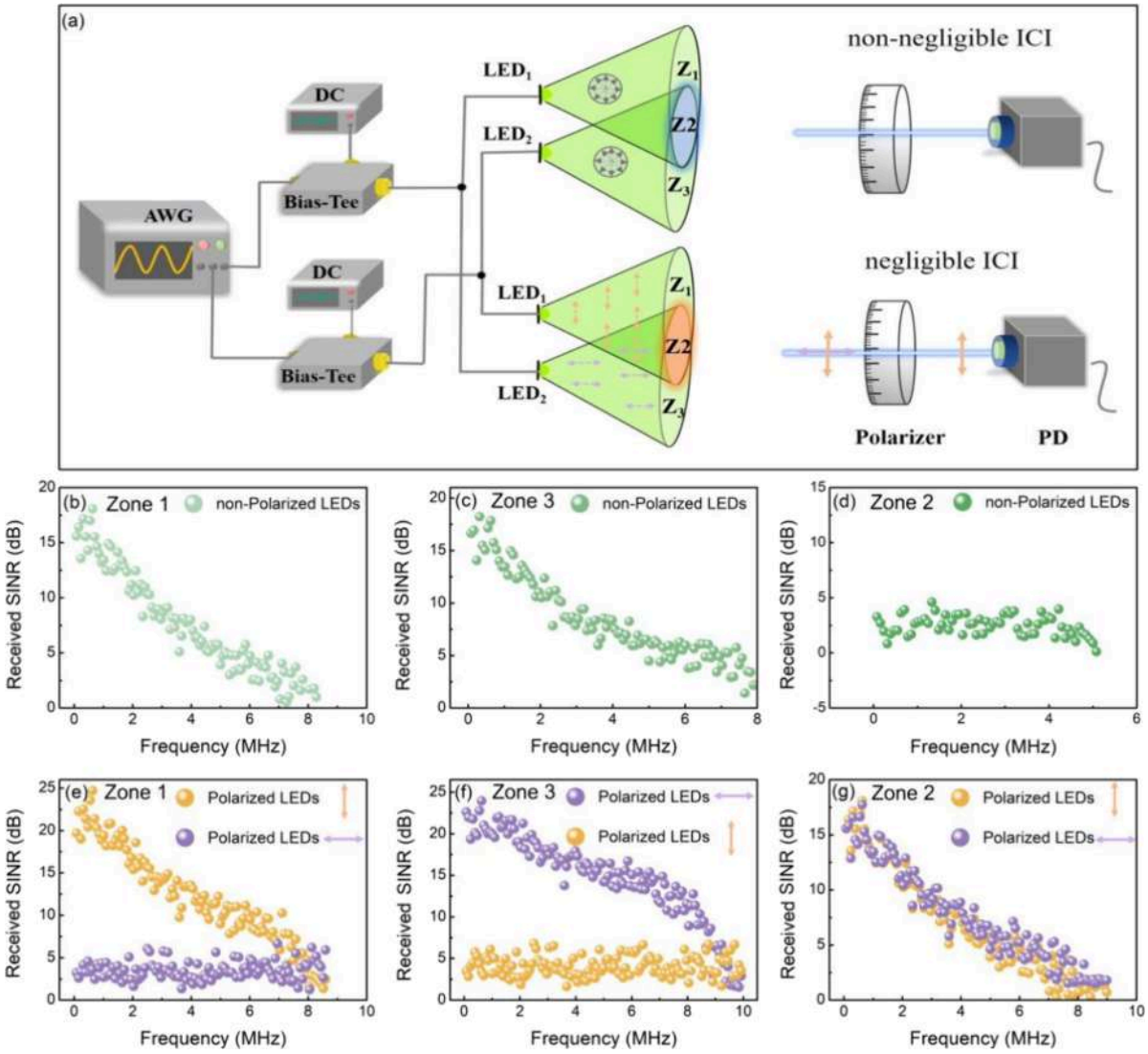


**Figure 5. (a) Schematic of the MC-VLC link including transmitting and receiving terminals using two PeLEDs and a polarizer-photodiode module. Received SINR variations with communication frequency based on nonpolarized PeLEDs in independent communication areas of (b) Zone 1 and (d) Zone 3 and overlapped area of (c) Zone 2. Received SINR variations with communication frequency based on polarized PeLEDs in independent communication areas of (e) Zone 1 and (g) Zone 3 and overlapped area of (f) Zone 2 at horizontal and perpendicular directions of the polarizer, respectively.**

The current density−luminescence−voltage ($J$−$L$−$V$) curves are exhibited in Figure 4a−c. The performance parameters are summarized in Table S4. The $J$−$V$ curves show that the current densities of P2 and C2 devices are higher than that of the P1 devices. Although the TMTA molecule itself acts as an insulator, it is noted that a very low concentration of TMTA solution in the solvent with a high boiling point solvent (i.e., 1.2 mg/mL in DMSO) is used for layer deposition, which is deemed to manifest an ultrathin TMTA layer. Thus, the leverage of TMTA as an insulator between PVK and the perovskite layer interface is deemed to be negligible. Rather, it benefits the orientational alignment of the perovskite crystal lattice, as well as interfacial defect passivation, both of which can enhance charge transport through the perovskite matrix. This can manifest increased carrier injection, thereby enhancing the current densities of P2 and C2 devices. The $L$−$V$ and EQE−$V$ curves show that the $L_{max}$ and EQ$E_{max}$ of the P1 device are only ∼7561 cd/m$^2$ and ∼9.5%, respectively. They increase to ∼23,960 cd/m$^2$ and ∼14.6% for the P2 device and further to ∼36,142 cd/m$^2$ and ∼23.7% for the C2 device, respectively. The EL spectra (Figure S11) show that the emission peaks of P1, P2, and C2 devices are almost identical, located at ∼512 nm. Moreover, these EL spectra are stable under different voltage bias. Finally, the half-lives of EL ($T_{50\text{-EL}}$) and EQE ($T_{50\text{-EQE}}$) at the initial luminance of ∼100 cd m$^{-2}$ are studied in Figure 4d,e to examine the stabilities of P1, P2, and C2 devices. The $T_{50\text{-EL}}$ and $T_{50\text{-EQE}}$ of the P1 device are only ∼0.5 and ∼0.9 h, respectively. For the P2 device, the $T_{50\text{-EL}}$ and $T_{50\text{-EQE}}$ values increase to ∼3.6 and ∼13.6 h, respectively. Compared with the P1 and P2 devices, the C2 device is the most stable, exhibiting the longest $T_{50\text{-EL}}$ and $T_{50\text{-EQE}}$ of ∼10.7 and ∼32.2 h, respectively.

To reveal the effects of oriented growth, defect passivation, and $n$-phase modulation of the quasi-2D perovskites on the performance of PeLEDs, the electrochemical impedance spectra (EIS) are employed to examine charge transport and recombination behaviors. Figure 4f shows the EIS of P1, P2, and C2 devices, and the inset shows the equivalent circuit for


https://doi.org/10.1021/acsnano.4c11761
ACS Nano XXXX, XXX, XXX−XXX

Nyquist plots including series resistance ($R_s$), recombination resistance ($R_{rec}$), and parallel capacitance ($C$).[55] $R_s$ is attributed to resistances at the device interfaces, and $R_{rec}$ is associated with the recombination resistance of the quasi-2D perovskite layer.[56] The fitting parameters presented in Table S5 indicate that the $R_s$ and $R_{rec}$ of the C2 device are the lowest among the P1, P2, and C2 devices, meaning the most efficient charge transport and higher radiation recombination rate in the C2 device.

The femtosecond transient absorption (fs-TA) spectra give deeper insights into the energy/charge carrier funneling and recombination within the multiquantum wells of quasi-2D perovskites.[33,51] As shown in Figure 4g−i, P1 and P2 samples exhibit distinctive ground-state bleach (GSB) peaks at ∼405, ∼435, ∼465, and ∼516 nm, corresponding to the excited states of $n$ = 1, 2, and 3 and $n \geq 4$ phases, respectively. But in the C2 sample, the peaks of ∼405, ∼435, and ∼465 nm are significantly weakened, leaving only one dominant peak at ∼516 nm. This is consistent with the steady-state UV−vis absorption spectra that the $n$ phases are modulated to $n \geq 4$ phases. Using multiexponential function eq 4, the dynamics of GSB signals of different $n$ phases (Figure 4j−l) are fitted:[33]

$$\Delta A(\tau) = A_1 e^{(-t/\tau_1)} + A_2 e^{(-t/\tau_2)} + A_3 e^{(-t/\tau_3)} + B_1 e^{(-t/\tau_{et})} \quad (4)$$

Here, $A_1$, $A_2$, $A_3$, and $B_1$ are amplitudes. $\tau_1$, $\tau_2$, and $\tau_3$ represent fast, medium, and slow decay time constants, respectively. $\tau_{et}$ is the formation time constant of the rising edge. In principle, $\tau_1$ of small-$n$ phases and $\tau_{et}$ of medium-$n$ phases are related to the energy/charge carrier funneling and generation of excited states, respectively.[57] By comparing the fitting parameters in Table S6, we see that $\tau_1$ of $n$ = 2 and 3 phases and $\tau_{et}$ of $n \geq 4$ phases continually decrease from the P1 and P2 to C2 samples, indicating faster energy/charge carrier funneling and generation of excited states facilitated by the oriented growth, defect passivation, and $n$-phase modulation.

To evaluate the linear polarization characteristics of the P1, P2, and C2 devices, the DoLPs of EL are measured by the experimental setup in Figure 4m. Under the luminance of ∼5000 cd m$^{-2}$, which is the minimum requirement in the scenario of MC-VLC, the DoLPs of P1, P2, and C2 devices are ∼0.9, ∼28, and ∼38%, respectively, as shown in Figure 4n. The increase in DoLP in EL aligns well with its enhancement in PL mode, confirming the establishment of aligned TMDs in the quasi-2D perovskites. The relatively lower DoLP of EL than that of PL is likely associated with the defect-induced dissipation processes of the injected carriers in EL operation (e.g., Joule heating and so on).[29,58,59] Notwithstanding, the C2 device still offers high performance and the polarized EL feature, corroborating the effectiveness of the synergistic coherence-programming strategy proposed in this study.

To validate the impacts of polarized EL exploitation on the MC-VLC applications, the demonstrated LP-PeLEDs are further employed as light sources for the MC-VLC link. We adopted an MC-VLC optical pathway, in which the transmitting and receiving terminals are composed of two PeLEDs and a polarizer-photodiode module, respectively (Figure 5a). To assess the communication capability of this MC-VLC link, the SINR variations with communication frequency of independent communication areas Zone 1 (LED1-controlled area) and Zone 3 (LED2-controlled area), as well as the overlapped area Zone 2, are measured.[60,61] When PeLEDs are nonpolarized (P1 device), the maximum SINRs of Zone 1 and Zone 3 are ∼18.1 and ∼17.8 dB, respectively, as shown in Figure 5b,c. However, the SINR significantly dropped to ∼5 dB in Zone 2, as shown in Figure 5d. This indicates that in overlapped Zone 2, the signals from the two nonpolarized PeLEDs interfere with each other, thereby reducing the communication capability of the MC-VLC link because the intercell interference (ICI) is non-negligible.[61]

Unlike the nonpolarized PeLEDs, which transmit signals in all directions, the polarized PeLEDs (C2 device) only transmit signals in one specific direction. In the C2 sample, this specific direction is ∼45° to the substrate (Figure S4) because the TDMs are aligned along this direction due to the oriented growth of the quasi-2D perovskite crystals (Figure 2j). Accordingly, two polarized PeLEDs are carefully positioned to ensure that their polarization directions are perpendicular to each other, realizing independent communications without interference (Figure S12). To see the improvements in communication capability from nonpolarized to polarized PeLEDs, the SINRs within Zone 1 and Zone 3 areas are measured. As shown in Figures S13 and S14, by rotating the polarizer in front of the photodiode (PD), the SINR remains almost unchanged for the nonpolarized PeLEDs. But for the polarized PeLEDs, the SINR changes significantly with the transmission direction. Especially, when the transmission direction of the polarizer is parallel to the polarization direction of LED1 but perpendicular to the polarization direction of LED2, the maximum SINR reaches to ∼24.7 dB in Zone 1 but reduces to ∼5.6 dB in Zone 3, as shown in Figure 5e. Also vice versa, the maximum SINR reaches ∼23.9 dB in Zone 3 but reduces to ∼6.8 dB in the Zone 1 area when the transmission direction of the polarizer is parallel to the polarization direction of LED2 but perpendicular to the polarization direction of LED1 (Figure 5f). This demonstrates that the on/off communication states of the two polarized PeLEDs can be intentionally selected by adjusting the transmission direction, avoiding interfered communications by two light sources.

By taking advantage of transmitting signals in a single direction, the polarized PeLEDs improve the communication capability in the overlapped Zone 2, as shown in Figure 5g. Unlike non-negligible ICI by using the nonpolarized PeLEDs, the polarized PeLEDs enable independent communications in Zone 2 with maximum SINRs of ∼18.1 and ∼17.7 dB, respectively. The maximum SINR is increased by ∼240% and shows negligible ICI in Zone 2 compared to the nonpolarized PeLEDs.

## CONCLUSIONS

In summary, we implemented a synergistic coherence-programming strategy to realize high-performance LP-PeLEDs. First, the TMTA layer is inserted at the PVK/perovskite interface, which guides the oriented growth of $[PbBr_6]^{4-}$ octahedron along the (110) plane. Additionally, the incorporation of 18-Crown-6 effectively passivates defects, further enhancing the DoLP of the PeLEDs. Finally, the $n$-phase distributions are also regulated, leading to optimized medium-$n$ phases that balance radiative recombination and DoLP. By establishing the aligned TDMs through these strategies, LP-PeLEDs with a maximum EQE of ∼23.7%, a maximum luminance of ∼36,142 cd/m$^2$, and a DoLP of ∼38% are fabricated, which also show potential in real MC-VLC applications. This work demonstrates the concurrent control of crystal orientation and transition dipole moments in


https://doi.org/10.1021/acsnano.4c11761
ACS Nano XXXX, XXX, XXX−XXX

realizing highly efficient and linearly polarized electroluminescence with quasi-2D perovskites, which has not been achieved so far.

Nevertheless, the inherent difficulty in (i) perfectly aligning (i.e., 100%) the crystallographic orientation and (ii) the inferior electrochemical stability of the polycrystalline perovskite thin films still brings the challenges to further improve its DoLP. Realization of a highly emissive, single-crystalline perovskite thin film, having an intrinsically high orientational alignment and low bulk defect densities, can be a potential breakthrough, which further requires extensive and specialized efforts.

## METHODS

**Materials.** Cesium bromide (CsBr, >99.999%) was purchased from Alfa Aesar. Lead bromide ($PbBr_2$, >99.99%) and phenethylammonium bromide (PEABr, >99.5%) were purchased from Xi'an Yuri Solar Co., Ltd. Trimethylolpropane triacrylate (TMTA, 85%, containing 600 ppm of MEHQ stabilizer) was purchased from CHONGQING YUEXIANG CHEMICAL CO., LTD. 1,4,7,10,13,16-Hexachlorocyclooctadecane (18-Crown-6 ether, >99.999%) was purchased from Sigma-Aldrich. Dimethyl sulfoxide (DMSO, >99.9%, GC) and chlorobenzene (CB, >99.9%, GC) were purchased from Aladdin. Poly(9-vinylcarbazole) (PVK, 99.99%, average $M_w \sim$ 90,000) and 1,3-tris (1-phenyl-19*H*-benzo[d]-imidazole-2-yl) benzene (TPBi, >99.99%) were purchased from Xi'an Yuri Solar Co., Ltd. 8-Hydroxy-quinolinatolithium (Liq, >99.99%) was purchased from Jilin OLED Material Tech Co., Ltd. All materials were used directly without further purification.

**Perovskite Precursor Solution.** The $PEA_2Cs_{n-1}Pb_nBr_{3n+1}$ perovskite precursor solution was prepared by dissolving CsBr, $PbBr_2$, and PEABr with the molar ratio of 1.2:1:0.3 in a DMSO solution with the total concentration of 10 wt %, in which the molar concentration of $Pb^{2+}$ is ~0.2 M. This mixture was then stirred at room temperature for 12 h in the glovebox (Dellix, LS-750S) with $H_2O$ and $O_2$ < 1.0 ppm. Simultaneously, 18-Crown-6 was dissolved in DMSO at 10, 20, and 30 mg/mL concentrations and also stirred at room temperature for 12 h. The 18-Crown-6 solutions were then mixed with the perovskite solution at a 1:25 volume ratio and stirred for an additional 4 h before use.

**PeLED Fabrications.** The structure of PeLEDs is ITO/PVK with or without a TMTA layer (40 nm)/$PEA_2Cs_{n-1}Pb_nBr_{3n+1}$ with or without 18-Crown-6 (40 nm)/TPBi (50 nm)/Liq (2.5 nm)/Al (90 nm). Initially, the prepatterned indium tin oxide (ITO, 15 $\Omega^{-1}$) glasses were successively cleaned in an ultrasonic bath using acetone, deionized water, and anhydrous ethanol and then dried in an oven. After ozone treatments, the ITO substrates were spin-coated with PVK HTL (6 mg/mL in CB) at 4000 rpm for 60 s and then annealed at 150 °C for 15 min. The TMTA layer (1.2 mg/mL in DMSO) was spin-coated on top of PVK at 5000 rpm for 30 s and annealed at 140 °C for 15 min. After cooling to room temperature, the perovskite layer was spin-coated at 4000 rpm for 60 s and then kept under a low pressure of $1 \times 10^{-1}$ Pa for 20 min. Finally, TPBi, Liq, and Al were sequentially evaporated through a shadow mask using an LN-1123SC organic/metal composite multisource evaporation system at a pressure $<3 \times 10^{-4}$ Pa. The active area is $2 \times 3$ $mm^2$.

**Characterizations.** The steady-state UV−vis absorption was measured on a Shimadzu UV-2600 spectrophotometer. A LifeSpec II Lifetime Spectrometer with a maximum average power of ~2 $\mu$W was used to measure the PL and TRPL of the perovskite film. The PLQE of perovskite films was measured by a Hamamatsu C11347-11 using a 445 nm diode. TEM was performed using a JELO JEM-2100 Plus. A Thermo Scientific K-Alpha+ XPS system was used for XPS analysis of Cs 3d, Pb 4f, and Br 3d chemical states. The excitation source was Al K$\alpha$ (1486.6 eV). FTIR spectroscopy was conducted by a BRUKER TENSOR 27. The XRD patterns were characterized by a Bruker D2PHASER. NMR spectra were recorded on Bruker Advance spectrometers (600 MHz for $^1$H). GIWAXS measurements were accomplished by a XOS Polycapillary X-ray Source. The incidence angle of the X-ray beam was set to be 1.0° for the perovskite films. GIWAXS patterns were recorded with a Pilatus 100 K detector. fs-TA spectroscopy was performed on a pump−probe system (Helios, Ultrafast System LLC) coupled with an amplified femtosecond laser system (Coherent) under ambient conditions. For the polarization-dependent PL measurement, the 405 nm laser is converted into circularly polarized light by a linear polarizer and a quarter-wave plate to excite the perovskite film. Subsequently, the laser and the emitted fluorescence pass through another polarizer and a 532 nm filter before reaching the photodetector and spectrometer. PL intensity was measured using an Ocean Optics USB2000+. EIS was measured on a CHI660D electrochemical workstation (CH Instrument Inc.). A 2 mV voltage amplitude was applied at an applied bias voltage of 3.5 V with frequencies between 1 MHz and 10 Hz under dark conditions. Z-view software was utilized for fitting the impedance spectra to derive the impedance parameters. *C*−*V* measurements were conducted by employing an all-in-one characterization platform (Paios, Fluxim AG) at 1 kHz with an AC amplitude of 20 mV. *C*−*F* measurements were also carried out in the Paios platform across a frequency range from 10 Hz to 10 MHz, employing an AC amplitude of 20 mV. The *J*−*L*−*V* characteristics of PeLEDs were carried out by a Keithley 2400 sourcemeter and luminance meter (KONICA, LS-110 colorimeter). Polarization-dependent EL was carried out by a Keithley 2400 and Ocean Optics USB2000+. For MC-VLC, two independent OFDM signals are generated using MATLAB and subsequently loaded onto a multichannel arbitrary waveform generator (AWG, Tektronix AFG31000 series). The signals from the AWG are then combined with an 8 V DC bias generated by a Keithley2400 precision power supply by using a bias tee to simultaneously load both. At a distance of 50 cm, the receiver simultaneously captures optical signals from both PeLEDs and converts them into electrical signals. These electrical signals are sampled using a digital storage oscilloscope (DSO, Tektronix MDO4054-3). Finally, the sampled signals are demodulated offline by using programmed MATLAB.

## ASSOCIATED CONTENT

### Supporting Information

The Supporting Information is available free of charge at https://pubs.acs.org/doi/10.1021/acsnano.4c11761.

Performance parameters of the reported LP-PeLEDs; photographs of TMTA before heating (TMTA monomers), TMTA after heating (cross-linked TMTA), and heated TMTA in DMSO; six periodic grid structures formed by cross-linking of TMTA monomers; relevant parameters of the DFT calculations for six TMTA periodic network structures; XRD patterns of P1, P2, and C2 samples; calculation method of orientational order parameter *S*; angle-dependent PL and EL intensities of P1 and P2 samples; schematic describing the experimental setup for measuring the DoLP of polarized PL; *C*−*V* and *C*−*f* curves of P2 and C2 devices; normalized TRPL decay curves and fitting parameters of P2 and C2 samples; PL spectra of quasi-2D perovskite films with different concentrations of 18-Crown-6; device structure of the fabricated PeLEDs; performance parameters of P1, P2, and C2 devices; EL spectra of P1, P2, and C2 devices under different voltages; EIS fitting parameters under dark conditions of P1, P2, and C2 devices; fitting parameters of fs-TA for P1, P2, and C2 samples; experimental setup for the MC-VLC system; received SINR with different polarizer angles in independent communication areas Zone 1 and Zone 3 based on nonpolarized and polarized PeLEDs (PDF)


https://doi.org/10.1021/acsnano.4c11761
ACS Nano XXXX, XXX, XXX−XXX

## AUTHOR INFORMATION


### Corresponding Authors

**Jonghee Yang** − *Department of Chemistry, Yonsei University, Seoul 03722, Republic of Korea;* orcid.org/0000-0001-7013-6761; Email: jhyang@yonsei.ac.kr

**Wei Zhang** − *Chongqing Institute of Green and Intelligent Technology, Chinese Academy of Sciences, Chongqing 400714, China;* orcid.org/0000-0002-9756-9994; Email: zhangwei@cigit.ac.cn

**Jidong Zhang** − *Changchun Institute of Applied Chemistry, Chinese Academy of Science, Changchun 130022, China;* Email: jdzhang@ciac.ac.cn

**Wenzhe Li** − *Institute of New Energy Technology, College of Physics & Optoelectronic Engineering, Jinan University, Guangzhou 510632, China;* orcid.org/0000-0002-7231-7686; Email: li_wz16@jnu.edu.cn

**Ping Chen** − *Chongqing Key Laboratory of Micro&Nano Structure Optoelectronics, School of Physical Science and Technology, Southwest University, Chongqing 400715, China;* orcid.org/0000-0003-0586-5970; Email: pingchen@swu.edu.cn

### Authors

**Meiqin Xiao** − *Chongqing Key Laboratory of Micro&Nano Structure Optoelectronics, School of Physical Science and Technology, Southwest University, Chongqing 400715, China*

**Long Xu** − *Chongqing Key Laboratory of Micro&Nano Structure Optoelectronics, School of Physical Science and Technology, Southwest University, Chongqing 400715, China;* orcid.org/0000-0002-3243-4087

**Chen Chen** − *School of Microelectronics and Communication Engineering, Chongqing University, Chongqing 400044, China;* orcid.org/0000-0003-2541-6283

**Tingwei Zhou** − *Chongqing Key Laboratory of Micro&Nano Structure Optoelectronics, School of Physical Science and Technology, Southwest University, Chongqing 400715, China;* orcid.org/0000-0002-5187-9567

**Haoyue Zhang** − *Chongqing Key Laboratory of Micro&Nano Structure Optoelectronics, School of Physical Science and Technology, Southwest University, Chongqing 400715, China*

**Bo Chen** − *Chongqing Key Laboratory of Micro&Nano Structure Optoelectronics, School of Physical Science and Technology, Southwest University, Chongqing 400715, China*

**Junzhong Wang** − *Chongqing Key Laboratory of Micro&Nano Structure Optoelectronics, School of Physical Science and Technology, Southwest University, Chongqing 400715, China;* orcid.org/0000-0003-1311-3736

Complete contact information is available at: https://pubs.acs.org/10.1021/acsnano.4c11761


### Author Contributions

M.X. carried out the device fabrication and characterizations and wrote the first draft of the manuscript. J.Y. revised the manuscript. L.X. set up the optical pathway for measuring the DoLP of EL and PL. W.Z. conceived the project funding and helped with TEM characterizations. J.Z. provided the GIWAXS facilities and performed the measurements. W.L. and T.Z. performed the DFT calculations on periodic structures of cross-linked TMTA. C.C. set up the two-cell OFDM-VLC system, and H.Z. helped with the MC-VLC measurements and analyzed the SINR data. B.C. helped with the film and device fabrications. J.W. helped and supervised M.X. P.C. conceived the idea and project funding, supervised the work, and made major revisions to the manuscript. All authors contributed to manuscript preparations and discussions.

### Notes

The authors declare no competing financial interest.

## ACKNOWLEDGMENTS

This work was financially supported by Fundamental Research Funds for the Natural Science Foundation Project of CQ CSTC (grant nos. CSTB2022NSCQ-MSX0438 and cstc2021jcyj-jqX0031), Interdiscipline Team Project under auspices of "Light of West" Program in Chinese Academy of Sciences (grant no. xbzg-zdsys-202106), Young Scholar of Regional Development Program in Chinese Academy of Sciences (grant no. 2021), National Natural Science Foundation of China (grant no. 22075103), Open Project of State Key Laboratory of Supramolecular Structure and Materials (grant no. sklssm 202405), and the Graduate Student Research Innovation Project of Chongqing (grant no. CYB240099). The authors acknowledge Dr. Lvpeng Yang from Wuhan National Laboratory for Optoelectronics, Huazhong University of Science and Technology for his kind help in analyzing the GIWAXS data.

## REFERENCES


(1) Chen, R.; Liang, N.; Zhai, T. Dual-Color Emissive OLED with Orthogonal Polarization Modes. *Nat. Commun.* **2024**, *15*, 1331.

(2) Wang, M.; Yang, Z.; Zhang, C. Polarized Photoluminescence from Lead Halide Perovskites. *Adv. Opt. Mater.* **2021**, *9*, No. 2002236.

(3) Geng, J. Three-Dimensional Display Technologies. *Adv. Opt. Photonics* **2013**, *5*, 456−535.

(4) Ge, Y.; Meng, L.; Bai, Z.; Zhong, H. Linearly Polarized Photoluminescence from Anisotropic Perovskite Nanostructures: Emerging Materials for Display Technology. *J. Inf. Dispersion* **2019**, *20*, 181−192.

(5) Fattal, D.; Peng, Z.; Tran, T.; Vo, S.; Fiorentino, M.; Brug, J.; Beausoleil, R. G. A. Multi-Directional Backlight for a Wide-Angle, Glasses-Free Three-Dimensional Display. *Nature* **2013**, *495*, 348−351.

(6) Jia, R.; Li, J.; Zhang, H.; Zhang, X.; Cheng, S.; Pan, J.; Wang, C.; Pirzado, A. A. A.; Dong, H.; Hu, W.; Jie, J.; Zhang, X. Highly Efficient Inherent Linearly Polarized Electroluminescence from Small-Molecule Organic Single Crystals. *Adv. Mater.* **2023**, *35*, No. 2208789.

(7) Zhou, L.; Zhou, Y.; Fan, B. L.; Nan, F.; Zhou, G. H.; Fan, Y. Y.; Zhang, W. J.; Ou, Q. D. Tailored Polarization Conversion and Light-Energy Recycling for Highly Linearly Polarized White Organic Light-Emitting Diodes. *Laser Photonics Rev.* **2020**, *14*, No. 1900341.

(8) Wu, J.; Fang, G.; Zhang, Y.; Biswas, N.; Ji, Y.; Xu, W.; Dong, B.; Liu, N. Semiconductor Nanomaterial-Based Polarized Light Emission: From Materials to Light Emitting Diodes. *Sci. China Mater.* **2023**, *66*, 1257−1282.

(9) Fu, X.; Mehta, Y.; Chen, Y. A.; Lei, L.; Zhu, L.; Barange, N.; Dong, Q.; Yin, S.; Mendes, J.; He, S.; Gogusetti, R.; Chang, C. H.; So, F. Directional Polarized Light Emission from Thin-Film Light-Emitting Diodes. *Adv. Mater.* **2021**, *33*, No. 2006801.

(10) Polyakov, A. Y.; Smirnov, N. B.; Govorkov, A. V.; Kim, J.; Ren, F.; Thaler, G. T.; Frazier, R. M.; Gila, B. P.; Abernathy, C. R.; Pearton, S. J.; Buyanova, I. A.; Rudko, G. Y.; Chen, W. M.; Pan, C.-C.; Chen, G.-T.; Chyi, J.-I.; Zavada, J. M. Electrical and Luminescent Properties and the Spectra of Deep Centers in GaMnN/InGaN Light-Emitting Diodes. *J. Electron. Mater.* **2004**, *33*, 241−247.

(11) Choi, G. J.; Van Le, Q.; Choi, K. S.; Kwon, K. C.; Jang, H. W.; Gwag, J. S.; Kim, S. Y. Polarized Light-Emitting Diodes Based on Patterned $MoS_2$ Nanosheet Hole Transport Layer. *Adv. Mater.* **2017**, *29*, No. 1702598.

(12) Quan, L. N.; García de Arquer, F. P.; Sabatini, R. P.; Sargent, E. H. Perovskites for Light Emission. *Adv. Mater.* **2018**, *30*, No. 1801996.
(13) Liu, X. K.; Xu, W.; Bai, S.; Jin, Y.; Wang, J.; Friend, R. H.; Gao, F. Metal Halide Perovskites for Light-Emitting Diodes. *Nat. Mater.* **2021**, *20*, 10−21.
(14) Lin, J.; Lu, Y.; Li, X.; Huang, F.; Yang, C.; Liu, M.; Jiang, N.; Chen, D. Perovskite Quantum Dots Glasses Based Backlit Displays. *ACS Energy Lett.* **2021**, *6*, 519−528.
(15) Chen, S.; Lin, J.; Zheng, S.; Zheng, Y.; Chen, D. Efficient and Stable Perovskite White Light-Emitting Diodes for Backlit Display. *Adv. Funct. Mater.* **2023**, *33*, No. 2213442.
(16) Zheng, S.; Wang, Z.; Jiang, N.; Huang, H.; Wu, X.; Li, D.; Teng, Q.; Li, J.; Li, C.; Li, J.; Pang, T.; Zeng, L.; Zhang, R.; Huang, F.; Lei, L.; Wu, T.; Yuan, F.; Chen, D. Ultralow Voltage-Driven Efficient and Stable Perovskite Light-Emitting Diodes. *Sci. Adv.* **2024**, *10*, No. eadp8473.
(17) Lin, J.; Chen, S.; Ye, W.; Zeng, Y.; Xiao, H.; Pang, T.; Zheng, Y.; Zhuang, B.; Huang, F.; Chen, D. Ultra-Stable Yellow Monolithic Perovskite Quantum Dots Film for Backlit Display. *Adv. Funct. Mater.* **2024**, *34*, No. 2314795.
(18) Chen, S.; Lin, J.; Huang, J.; Pang, T.; Ye, Q.; Zheng, Y.; Li, X.; Yu, Y.; Zhuang, B.; Chen, D. $CsPbBr_3$@Glass Nanocomposite with Green-Emitting External Quantum Efficiency of 75% for Backlit Display. *Adv. Funct. Mater.* **2024**, *34*, No. 2309293.
(19) Liu, E.; Zhang, H.; Fu, H. Tailoring Pure-Phase Quasi-2D Perovskites via the Polymer Crystallization-Assisted Strategy. *Chem. Mater.* **2024**, *36*, 5370−5377.
(20) Wang, M.; Tang, J.; Wang, H.; Zhang, C.; Zhao, Y. S.; Yao, J. Grain Boundary Enhanced Photoluminescence Anisotropy in Two-Dimensional Hybrid Perovskite Films. *Adv. Opt. Mater.* **2020**, *8*, No. 1901780.
(21) Gao, Y.; Zhao, L.; Shang, Q.; Zhong, Y.; Liu, Z.; Chen, J.; Zhang, Z.; Shi, J.; Du, W.; Zhang, Y.; Chen, S.; Gao, P.; Liu, X.; Wang, X.; Zhang, Q. Ultrathin $CsPbX_3$ Nanowire Arrays with Strong Emission Anisotropy. *Adv. Mater.* **2018**, *30*, No. 1801805.
(22) Lee, J.-W.; Park, N.-G. Quasi-Two-Dimensional Perovskite Light Emitting Diodes for Bright Future. *Light: Sci. Appl.* **2021**, *10*, 86.
(23) Li, J.; Ma, J.; Cheng, X.; Liu, Z.; Chen, Y.; Li, D. Anisotropy of Excitons in Two-Dimensional Perovskite Crystals. *ACS Nano* **2020**, *14*, 2156−2161.
(24) Lin, C. H.; Kang, C. Y.; Wu, T. Z.; Tsai, C. L.; Sher, C. W.; Guan, X.; Lee, P. T.; Wu, T.; Ho, C. H.; Kuo, H. C.; He, H. Jr. Giant Optical Anisotropy of Perovskite Nanowire Array Films. *Adv. Funct. Mater.* **2020**, *30*, No. 1909275.
(25) Ghoshal, D.; Wang, T.; Tsai, H. Z.; Chang, S. W.; Crommie, M.; Koratkar, N.; Shi, S. F. Catalyst-Free and Morphology-Controlled Growth of 2D Perovskite Nanowires for Polarized Light Detection. *Adv. Opt. Mater.* **2019**, *7*, No. 1900039.
(26) Ye, J.; Ren, A.; Dai, L.; Baikie, T. K.; Guo, R.; Pal, D.; Gorgon, S.; Heger, J. E.; Huang, J.; Sun, Y.; Arul, R.; Grimaldi, G.; Zhang, K.; Shamsi, J.; Huang, Y. T.; Wang, H.; Wu, J.; Koenderink, A. F.; Torrente Murciano, L.; Schwartzkopf, M.; et al. Direct Linearly Polarized Electroluminescence from Perovskite Nanoplatelet Superlattices. *Nat. Photonics.* **2024**, *18*, 586−5.
(27) Lu, W. G.; Wu, X. G.; Huang, S.; Wang, L.; Zhou, Q.; Zou, B.; Zhong, H.; Wang, Y. Strong Polarized Photoluminescence from Stretched Perovskite-Nanocrystal-Embedded Polymer Composite Films. *Adv. Opt. Mater.* **2017**, *5*, No. 1700594.
(28) Meng, L.; Yang, C.; Meng, J.; Wang, Y.; Ge, Y.; Shao, Z.; Zhang, G.; Rogach, A. L.; Zhong, H. *In-Situ* Fabricated Anisotropic Halide Perovskite Nanocrystals in Polyvinylalcohol Nanofibers: Shape Tuning and Polarized Emission. *Nano Res.* **2019**, *12*, 1411−1416.
(29) Wei, Y.; Xu, Y.; Wang, Q.; Wang, J.; Lu, H.; Zhu, J. $CsPbBr_3$ Nanowire Polarized Light-Emitting Diodes through Mechanical Rubbing. *Chem. Commun.* **2020**, *56*, 5413−5416.
(30) Li, L.; Hu, Y.; Chen, Y.; Wang, C.; Zhao, G.; Du, X.; Wang, C.; Xiao, L.; Lu, Z.; Wang, J.; Wang, D.; Jie, J.; Huang, J.; Zou, G. Surface Defect Suppression for High Color Purity Light-Emitting Diode of Free-Standing Single-Crystal Perovskite Film. *Adv. Funct. Mater.* **2023**, *33*, No. 2301205.
(31) Jiang, Y.; Cui, M.; Li, S.; Sun, C.; Huang, Y.; Wei, J.; Zhang, L.; Lv, M.; Qin, C.; Liu, Y.; Yuan, M. Reducing the Impact of Auger Recombination in Quasi-2D Perovskite Light-Emitting Diodes. *Nat. Commun.* **2021**, *12*, 336.
(32) Zhang, L.; Sun, C.; He, T.; Jiang, Y.; Wei, J.; Huang, Y.; Yuan, M. High-Performance Quasi-2D Perovskite Light-Emitting Diodes: From Materials to Devices. *Light: Sci. Appl.* **2021**, *10*, 61.
(33) Yang, L.; Zhang, Y.; Ma, J.; Chen, P.; Yu, Y.; Shao, M. Pure Red Light-Emitting Diodes Based on Quantum Confined Quasi-Two-Dimensional Perovskites with Cospacer Cations. *ACS Energy Lett.* **2021**, *6*, 2386−2394.
(34) Yuan, M.; Quan, L. N.; Comin, R.; Walters, G.; Sabatini, R.; Voznyy, O.; Hoogland, S.; Zhao, Y.; Beauregard, E. M.; Kanjanaboos, P.; Lu, Z.; Kim, D. H.; Sargent, E. H. Perovskite Energy Funnels for Efficient Light-Emitting Diodes. *Nat. Nanotechnol.* **2016**, *11*, 872−877.
(35) Chen, Y.; Yu, S.; Sun, Y.; Liang, Z. Phase Engineering in Quasi-2D Ruddlesden-Popper Perovskites. *J. Phys. Chem. Lett.* **2018**, *9*, 2627−2631.
(36) Yang, X.; Zhang, X.; Deng, J.; Chu, Z.; Jiang, Q.; Meng, J.; Wang, P.; Zhang, L.; Yin, Z.; You, J. Efficient Green Light-Emitting Diodes Based on Quasi-Two-Dimensional Composition and Phase Engineered Perovskite with Surface Passivation. *Nat. Commun.* **2018**, *9*, 570.
(37) Qin, J.; Zhang, J.; Shen, T.; Wang, H.; Hu, B.; Gao, F. Aligning Transition Dipole Moment toward Light Amplification and Polarized Emission in Hybrid Perovskites. *Adv. Opt. Mater.* **2021**, *9*, No. 2100984.
(38) Wang, D.; Wu, D.; Dong, D.; Chen, W.; Hao, J.; Qin, J.; Xu, B.; Wang, K.; Sun, X. Polarized Emission from $CsPbX_3$ Perovskite Quantum Dots. *Nanoscale* **2016**, *8*, 11565−11570.
(39) Wang, S.; Yu, Z.; Qin, J.; Chen, G.; Liu, Y.; Fan, S.; Ma, C.; Yao, F.; Cui, H.; Zhou, S.; Dong, K.; Lin, Q.; Tao, C.; Gao, F.; Ke, W.; Fang, G. Buried Interface Modification and Light Outcoupling Strategy for Efficient Blue Perovskite Light-Emitting Diodes. *Sci. Bull.* **2024**, *69*, 2231−2240.
(40) Caiazzo, A.; Datta, K.; Bellini, L.; Wienk, M. M.; Janssen, R. A. J. Impact of Alkyl Chain Length on the Formation of Regular - and Reverse-Graded Quasi-2D Perovskite Thin Films. *ACS Mater. Lett.* **2024**, *6*, 267−274.
(41) Song, H.; Kim, H. B.; Cho, S. C.; Lee, J.; Yang, J.; Jeong, W. H.; Won, J. Y.; Jeong, H. I.; Yeop, J.; Kim, J. Y.; Lawrie, B. J.; Ahmadi, M.; Lee, B. R.; Kim, M.; Choi, S. J.; Kim, D. S.; Lee, M.; Lee, S. U.; Jo, Y.; Choi, H. Supramolecular Design Principles in Pseudohalides for High-Performance Perovskite Solar Mini Modules. *Joule* **2024**, *8*, 2283−2303.
(42) Yang, J.; Lawrie, B. J.; Kalinin, S. V.; Ahmadi, M. High-Throughput Automated Exploration of Phase Growth Behaviors in Quasi-2D Formamidinium Metal Halide Perovskites. *Adv. Energy Mater.* **2023**, *13*, No. 2302337.
(43) Chen, B.; Liu, H.; Yang, J.; Ahmadi, M.; Chen, Q.; Yin, N.; Zhang, S.; Xiao, M.; Zhang, H.; Xu, L.; Chen, P. Coordination of Thermally Activated Delayed Fluorescent Molecules for Efficient and Stable Perovskite Light-Emitting Diodes. *Adv. Funct. Mater.* **2024**, *34*, No. 2402522.
(44) Yang, G.; Liu, X.; Wang, L.; Dong, K.; Zhang, B.; Jiang, X.; Yin, Y.; Wang, M.; Niu, W.; Zheng, L.; Yu, S.; Liu, S.; Zakeeruddin, S. M.; Guo, X.; Pang, S.; Sun, L.; Grätzel, M.; Wei, M. Tailored Supramolecular Interactions in Host-Guest Complexation for Efficient and Stable Perovskite Solar Cells and Modules. *Angew. Chem., Int. Ed.* **2024**, No. e202410454.
(45) Yang, L.; Shi, J.; Wu, Y.; Jin, X.; Bie, T.; Hu, C.; Liang, W.; Gao, Y.; Xu, M.; Shao, M. Long Carrier Diffusion Length and Efficient Charge Transport in Thick Quasi-Two-Dimensional Perovskite Solar Cells Enabled by Modulating Crystal Orientation and Phase Distribution. *ACS Appl. Energy Mater.* **2022**, *5*, 8930−8939.


https://doi.org/10.1021/acsnano.4c11761
ACS Nano XXXX, XXX, XXX−XXX

(46) Liu, Z.; Qiu, W.; Peng, X.; Sun, G.; Liu, X.; Liu, D.; Li, Z.; He, F.; Shen, C.; Gu, Q.; Ma, F.; Yip, H. L.; Hou, L.; Qi, Z.; Su, S. J. Perovskite Light-Emitting Diodes with EQE Exceeding 28% through a Synergetic Dual-Additive Strategy for Defect Passivation and Nanostructure Regulation. *Adv. Mater.* **2021**, *33*, No. 2103268.

(47) Walters, G.; Haeberlé, L.; Quintero-Bermudez, R.; Brodeur, J.; Kéna-Cohen, S.; Sargent, E. H. Directional Light Emission from Layered Metal Halide Perovskite Crystals. *J. Phys. Chem. Lett.* **2020**, *11*, 3458−3465.

(48) Ren, Z.; Yu, J.; Qin, Z.; Wang, J.; Sun, J.; Chan, C. C. S.; Ding, S.; Wang, K.; Chen, R.; Wong, K. S.; Lu, X.; Yin, W.; Choy, W. C. H. High-Performance Blue Perovskite Light-Emitting Diodes Enabled by Efficient Energy Transfer between Coupled Quasi-2D Perovskite Layers. *Adv. Mater.* **2021**, *33*, No. 2005570.

(49) Chen, P.; Xiong, Z.; Wu, X.; Shao, M.; Ma, X.; Xiong, Z. H.; Gao, C. Highly Efficient Perovskite Light-Emitting Diodes Incorporating Full Film Coverage and Bipolar Charge Injection. *J. Phys. Chem. Lett.* **2017**, *8*, 1810−1818.

(50) Xu, Y.; Tang, Z.; Guo, Y.; Wang, Q.; Chen, L.; Chen, H.; Wang, D.; Xie, Z. High-Efficiency Quasi-2D Perovskite Light-Emitting Diodes Using a Dual-Additive Strategy Guided by Preferential Additive-Precursor Interactions. *Adv. Opt. Mater.* **2023**, *11*, No. 2202808.

(51) Xiang, T.; Li, T.; Wang, M.; Zhang, W.; Ahmadi, M.; Wu, X.; Xu, T.; Xiao, M.; Xu, L.; Chen, P. 12-Crown-4 Ether Assisted in-Situ Grown Perovskite Crystals for Ambient Stable Light Emitting Diodes. *Nano Energy* **2022**, *95*, No. 107000.

(52) Ng, Y. F.; Kulkarni, S. A.; Parida, S.; Jamaludin, N. F.; Yantara, N.; Bruno, A.; Soci, C.; Mhaisalkar, S.; Mathews, N. Highly Efficient Cs-Based Perovskite Light-Emitting Diodes Enabled by Energy Funnelling. *Chem. Commun.* **2017**, *53*, 12004−12007.

(53) Shang, Y.; Li, G.; Liu, W.; Ning, Z. Quasi-2D Inorganic $CsPbBr_3$ Perovskite for Efficient and Stable Light-Emitting Diodes. *Adv. Funct. Mater.* **2018**, *28*, No. 1801193.

(54) Kong, L.; Zhang, X.; Li, Y.; Wang, H.; Jiang, Y.; Wang, S.; You, M.; Zhang, C.; Zhang, T.; Kershaw, S. V.; Zheng, W.; Yang, Y.; Lin, Q.; Yuan, M.; Rogach, A. L.; Yang, X. Smoothing the Energy Transfer Pathway in Quasi-2D Perovskite Films Using Methanesulfonate Leads to Highly Efficient Light-Emitting Devices. *Nat. Commun.* **2021**, *12*, 1246.

(55) Von Hauff, E.; Klotz, D. Impedance Spectroscopy for Perovskite Solar Cells: Characterisation, Analysis, and Diagnosis. *J. Mater. Chem. C* **2022**, *10*, 742−761.

(56) Zhang, H.; Ye, F.; Li, W.; Gurney, R. S.; Liu, D.; Xiong, C.; Wang, T. Improved Performance of Perovskite Light-Emitting Diodes by Dual Passivation with an Ionic Additive. *ACS Appl. Energy Mater.* **2019**, *2*, 3336−3342.

(57) Qin, C.; Xu, L.; Zhou, Z.; Song, J.; Ma, S.; Jiao, Z.; Jiang, Y. Carrier Dynamics in Two-Dimensional Perovskites: Dion-Jacobson: Vs. Ruddlesden-Popper Thin Films. *J. Mater. Chem. A* **2022**, *10*, 3069−3076.

(58) Liu, M.; Wan, Q.; Wang, H.; Carulli, F.; Sun, X.; Zheng, W.; Kong, L.; Zhang, Q.; Zhang, C.; Zhang, Q.; Brovelli, S.; Li, L. Suppression of Temperature Quenching in Perovskite Nanocrystals for Efficient and Thermally Stable Light-Emitting Diodes. *Nat. Photonics* **2021**, *15*, 379−385.

(59) Li, N.; Jia, Y.; Guo, Y.; Zhao, N. Ion Migration in Perovskite Light-Emitting Diodes: Mechanism, Characterizations, and Material and Device Engineering. *Adv. Mater.* **2022**, *34*, No. 2108102.

(60) Ryoo, H. N.; Kwon, D. H.; Yang, S. H.; Han, S. K. Differential Optical Detection in VLC for Inter-Cell Interference Reduced Flexible Cell Planning. *IEEE Photonics Technol. Lett.* **2016**, *28*, 2728−2731.

(61) Chen, C.; Zhong, W. De; Yang, H.; Zhang, S.; Du, P. Reduction of SINR Fluctuation in Indoor Multi-Cell VLC Systems Using Optimized Angle Diversity Receiver. *J. Lightwave Technol.* **2018**, *36*, 3603−3610.



https://doi.org/10.1021/acsnano.4c11761
*ACS Nano* XXXX, XXX, XXX−XXX